# High-output soft-contact fiber-structure triboelectric nanogenerator and its sterilization application

IOP Publishing Nanotechnology
Nanotechnology 34 (2023) 385403 (12pp) https://doi.org/10.1088/1361-6528/acdfd5

# High-output soft-contact fiber-structure triboelectric nanogenerator and its sterilization application

**Jianwei He[1,5], Xuhua Guo[1,5], Caofeng Pan[2], Gang Cheng[3], Mingli Zheng[3], Yunlong Zi[4], Hongzhi Cui[1,*] and Xiaoyi Li[1,3,*]**

[1] College of Materials Science and Engineering, Ocean University of China, Qingdao 266100, People's Republic of China
[2] Beijing Institute of Nanoenergy and Nanosystems, Chinese Academy of Sciences, Beijing 101400, People's Republic of China
[3] Key Lab for Special Functional Materials of Ministry of Education, School of Materials Science and Engineering, Henan University, Kaifeng, 475004, People's Republic of China
[4] Sustainable Energy and Environment Thrust, Hong Kong University of Science and Technology, Guangzhou, 510000, People's Republic of China

E-mail: cuihongzhi@ouc.edu.cn and lixiaoyi@ouc.edu.cn

Received 30 January 2023, revised 24 April 2023
Accepted for publication 20 June 2023
Published 6 July 2023

**Abstract**

Infectious diseases are spreading rapidly with the flow of the world's population, and the prevention of epidemic diseases is particularly important for public and personal health. Therefore, there is an urgent need to develop a simple, efficient and non-toxic method to control the spread of bacteria and viruses. The newly developed triboelectric nanogenerator (TENG) can generate a high voltage, which inhibits bacterial reproduction. However, the output performance is the main factor limiting real-world applications of TENGs. Herein, we report a soft-contact fiber-structure TENG to avoid insufficient friction states and to improve the output, especially at a high rotation speed. Rabbit hair, carbon nanotubes, polyvinylidene difluoride film and paper all contain fiber structures that are used to guarantee soft contact between the friction layers and improve the contact state and abrasion problem. Compared with a direct-contact triboelectric nanogenerator, the outputs of this soft-contact fiber-structure TENG are improved by about 350%. Meanwhile, the open-circuit voltage can be enhanced to 3440 V, which solves the matching problems when driving high-voltage devices. A TENG-driven ultraviolet sterilization system is then developed. The bactericidal rate of this sterilization system can reach 91%, which significantly reduces the risk of disease spread. This work improves a forward-looking strategy to improve the output and service life of the TENG. It also expands the applications of self-powered TENG sterilization systems.

Supplementary material for this article is available online

Keywords: triboelectric nanogenerator, fiber-structure materials, high voltage output, sterilization

(Some figures may appear in colour only in the online journal)

## 1. Introduction

In the long history of humankind, infectious diseases caused by bacteria and viruses have brought many disasters [1, 2].

[5] Two authors contributed equally to this work.
[*] Authors to whom any correspondence should be addressed.

 

Even today, when science and medical treatment are relatively developed, infectious diseases are still one of our most threatening challenges [3–7]. Bacteria and viruses can easily spread from person to person through the air, for example SARS [8–10], avian influenza [11, 12], measles [13], epidemic cerebrospinal meningitis [14], pulmonary tuberculosis [15, 16], COVID-19 [17], etc. Frequent disinfection of the environment is one of the effective means to avoid the spread of diseases and ensure health and safety. At present, sterilization and disinfection of the family environment mainly include physical disinfection and chemical disinfection. Toxic chemicals used for chemical disinfection, such as peracetic acid and sodium hypochlorite, are generally corrosive and easily leave residues that are not only harmful to people's health but also the ecological environment [18, 19]. Ultraviolet disinfection has become an increasingly popular physical disinfection technology due to its advantages of safety, efficiency and no secondary pollution. However, the dependence on a stable power grid system and a complex boost circuit severely limits Ar–Hg lamps. It is difficult to apply ultraviolet sterilization systems in remote areas and outdoor environments without a power supply. Therefore, it is necessary to develop an independent and environmentally friendly ultraviolet light source for disinfection, which is independent of the power grid and can be used in households and other environments to ensure human health and safety.

A triboelectric nanogenerator (TENG), based on a coupling of the triboelectric effect and electrostatic induction, can effectively convert various environmental mechanical movements into electrical energy [20–22]. Recently, this new power technology has been developed for many purposes, such as micro power supplies [23–26], blue energy [27–31] and self-powered sensors [32–36], showing great significance and prospects for application in many fields. TENGs not only have the advantages of low-frequency mechanical energy trapping, high efficiency and low cost, but they have also attracted more and more attention for safe high-voltage applications due to their unique high-voltage and low-current output characteristics [37–39]. In recent years, more and more TENG research has focused on sterilization, but most are only applied to small-scale water sterilization and there are few reports that they can be applied in various environments for large-scale sterilization [40–42]. The output performance of a TENG is one of the most important indicators. Among TENGs with various structures, a rotary triboelectric nanogenerator (R-TENG) has the advantages of high efficiency and continuous output compared with other structures [43]. Researchers have also found that increasing the area of the contact surface is one of the effective means to improve the output of a TENG [44]. However, mechanical abrasion and heat of the friction layer will reduce the output performance of the device and lead to poor mechanical stability during a long period of work. The service life of a TENG is seriously affected, and new devices need to be replaced frequently to maintain good output efficiency. In addition, the macromolecular polymers often used as friction layers will also have certain effects on the environment. To reduce the mechanical abrasion between friction layers and improve the service life of a R-TENG, non-contact triboelectric nanogenerators (NC-TENG) have been invented [45–49]. In NC-TENGs, abrasion is avoided but the charge on the dielectric surface will gradually dissipate over time due to lack of a timely supplement. The rate of dissipation depends on the ability of the dielectric material to retain surface charges. The reduction of surface charge density will have a huge impact on the output performance. For a TENG with contact mode and non-contact mode switching under specific conditions, the abrasion between media also cannot be avoided, and stability of the equipment and output will be reduced during working mode switching. Given this, it is very necessary to develop a long-life, high-performance, stable-output TENG as a high-voltage power supply in practical applications.

This paper reports a soft-contact, high-output, high-stability R-TENG based on fibrous materials, its structural designs and circuit management. Degradable materials with a fiber structure, including rabbit hair, paper, and carbon nanotubes (CNTs), are introduced into the TENG device, and the loose and porous fiber structures are more conducive to the adhesion of bacteria, which will significantly enhance the degradability of materials and reduce the environmental pollution. Compared with materials without surface structure, fiber-structured materials with a larger surface area can bring higher output performance to TENG. In addition, a soft-contact design is used to guarantee a sufficient friction state and high outputs in high rotation speed, and it also avoids the abrasion problem and thus enlarges TENG's lifetime. Compared with the direct-contact TENG, the outputs of this soft-contact fiber-structure TENG are improved by at least 350% at high speed. With the help of circuit management, 3440 V DC voltage can be easily obtained, and the matching problem with commercial electron devices is also solved. Finally, a TENG-driven ultraviolet sterilization system is developed for home, school, and other environments for daily disinfection and sterilization. The bactericidal rate of this sterilization system can reach 91%, which significantly reduces the risk of disease breeding. This work provides a useful idea for the structural design of a TENG, and it opens up a new way for infectious disease control and a self-powered sterilization system, especially in isolated or remote areas.

## 2. Results and discussion

### *2.1. Device structure and schematic of the soft-contact R-TENG*

Figure 1(a) presents the hierarchical structure of a TENG, which consists of two parts, a rotor and a stator. The rotor part is based on an acrylic substrate. Polyvinylidene difluoride (PVDF) is attached to the acrylic substrate via electrospinning as the first triboelectric dielectric. Then, the electrospun PVDF film is divided into six equal-sized sectors by laser cutting. Half of the fan-shaped PVDF films are removed and the remaining counterparts alternately distributed on the acrylic surface. The blank parts are filled with paper as the second triboelectric medium. A rotor with PVDF and paper

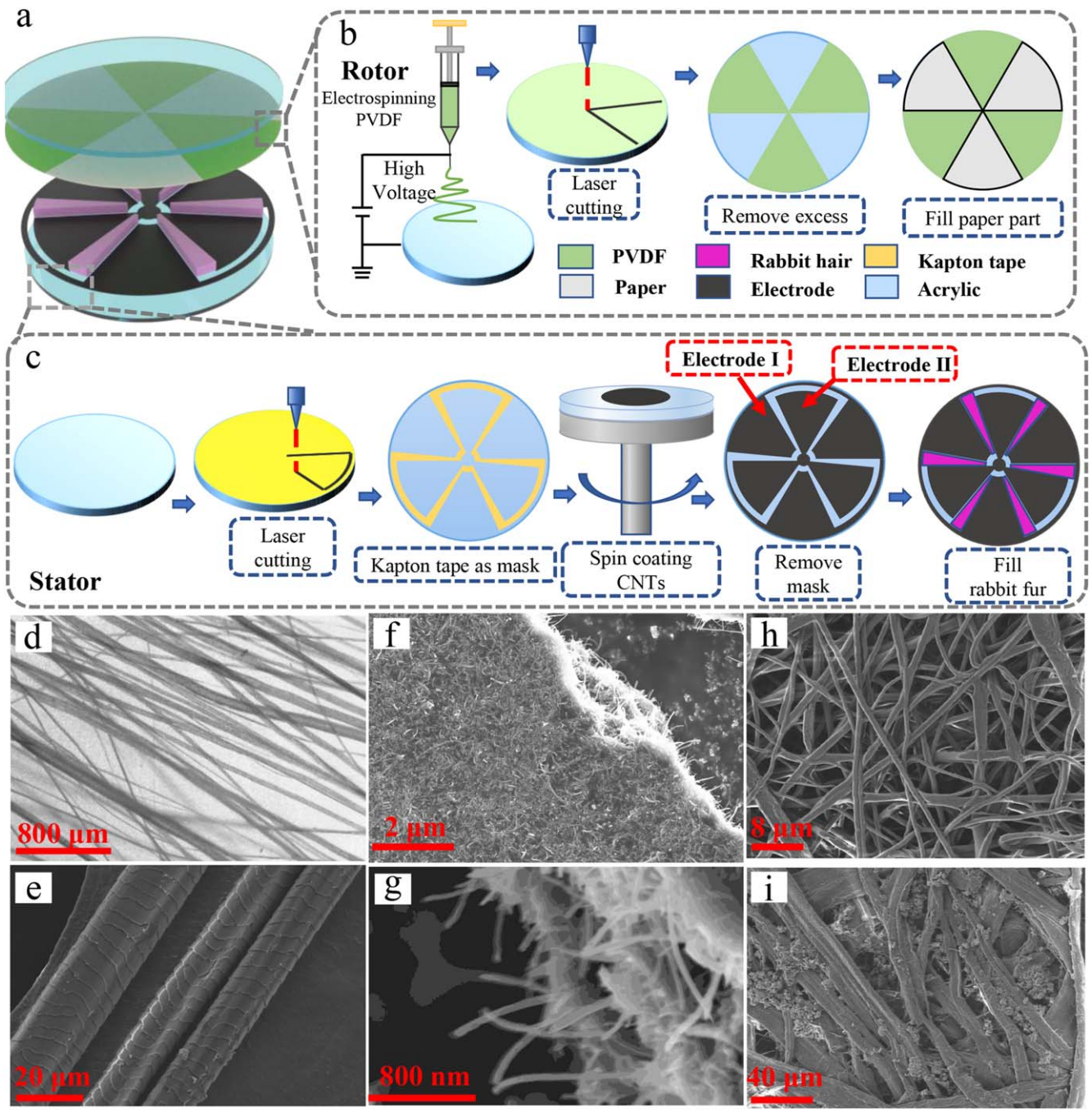


**Figure 1.** Structure and schematic of a soft-contact R-TENG. (a) Hierarchical structure diagram of the soft-contact R-TENG. (b) The manufacturing process of the rotor. (c) The manufacturing process of the stator. (d) Photographs of rabbit hair. The scale bar is 800 $\mu$m. (e) SEM image of the rabbit hair scale structure. The scale bar is 20 $\mu$m. (f), (g) SEM image of CNTs and enlarged view of a local section. Scale bars are 2 $\mu$m and 800 nm. (h) SEM image of PVDF electrospinning fiber film. The scale bar is 2 $\mu$m. (i) SEM images of the paper surface. The scale bar is 40 $\mu$m.

alternately attached to the acrylic substrate is obtained. For the stator part, an acrylic plate is used as the base as for the rotor part. The Kapton tape, which is glued to the substrate, is laser cut with an accurate mask pattern. Then the excess is removed, leaving a mask on the acrylic sheet. The CNT solution is spin coated on the substrate with a mask as the electrode material. After the slurry has dried, the mask is removed. Two electrodes with regular shapes were obtained. The electrodes associated internally are defined as electrode 1. The counterpart of the external connection is called electrode 2. As the third kind of friction dielectric, rabbit hair is used to fill in the electrode gap; its triboelectric property between paper and PVDF can effectively supplement the charge for the other two friction media in time. The TENG's soft-contact and sufficient friction are realized by soft and fluffy rabbit hair. Figures 1(b) and (c) show the details of the rotor and stator preparation process. Figure 1(d) presents a micrograph of rabbit hair. A higher magnification image of

rabbit hair shown in figure 1(e), in which the scale structure of the hair can be seen. The scanning electron microscope (SEM) image of CNTs, which comprise the electrode material, is shown in figure 1(f). The tubular structure is visible in figure 1(g) with larger magnification. A SEM micrograph of PVDF electrospinning fiber film is shown in figure 1(h); the fiber thickness is about 1 $\mu$m. The microscopic image of the paper is shown in figure 1(i). It can be seen in the figure that the fiber thickness varies greatly, the edge is relatively rough and there are many small particles on the surface. This also reflects the roughness of the paper surface from the microstructure. Whether rabbit hair, PVDF film or paper, the friction area is effectively increased by their fiber structure to ensure high-performance output of the TENG. At the same time, the loose and porous fiber structure of these degradable materials is more conducive to the adhesion of bacteria on the surface of materials, thus accelerating the degradability of materials.

### *2.2. Working mechanism of the TENG*

The abrasion of friction materials is still a serious challenge for the practical application of long-term energy collection. The non-contact TENG can effectively solve the problem of abrasion, but in the long-term non-contact friction in the medium will lead to charge dissipation, which will seriously reduce the output power of the TENG. To improve mechanical durability and output efficiency of the TENG, a soft-contact triboelectric nanogenerator based on rabbit hair was designed. Because the fluffy rabbit hair has a certain elasticity and softness, the friction layer will not contact the electrode and be abraded. In addition, the frictional electrical properties of the three friction media can be determined by measuring the surface potential after mutual contact. PVDF is more likely to obtain negative charges and paper is more likely to obtain positive charges. The order from positive to negative frictional properties is paper, rabbit hair and PVDF film. Therefore, the rabbit hair always acts as a charge transfer station, because its charge affinity is between that of PVDF and paper. When the soft-contact TENG starts to work, the hair receives electrons from the paper and transfers them to the PVDF with stronger electronegativity when it contacts the PVDF. At the same time, the stronger electronegativity will also deprive the hair of some electrons until the frictional charge density of paper and PVDF is saturated. A comparison of friction electronegativity and output between rabbit hair, paper and PVDF is shown in figure S1. A cross-section diagram of the working state is shown in figure 2(a). PVDF will have a negative charge due to its triboelectricity; on the contrary, the paper will have a positive charge. The corresponding two electrode parts induce the same number of opposite charges. With the rotation of the rotor part, the corresponding positions of the electrode and the two media on the rotor change, and the induced positive charge on electrode 1 decreases and flows to electrode 2. The current direction is from electrode 1 to electrode 2. As the charge affinity of the hair is between that of the paper and PVDF, the charge loss of the paper will be replenished when it contacts the hair, and it will return to the state of charge saturation. Figures 2(b) and (c) shows this process. When electrode 1 corresponds to the position of the paper and electrode 2 corresponds to the position of the PVDF film (i.e. Figure 2(f)), half of a current cycle ends. The continuous rotation of the rotor makes the current between the two electrodes opposite to the preceding direction. At the same time, the negatively charged rabbit hair rubbing against the paper is in contact with the PVDF medium. If the charge on PVDF film is dissipated, then the negative charge carried by rabbit hair will be added to PVDF to maintain its original charge density. This process is shown in figure 2(e). The rotor continues to rotate until it returns from the position in figure 2(d) to the original position (figure 2(a)), and one current cycle is completed.

The sketches and finite element simulation by COMSOL are utilized to demonstrate the open-circuit voltage, as shown in figures 2(g)–(j). In the charge saturation state of the friction layer, electrode 1 is aligned with the position of the PVDF and electrode 2 is aligned with the position of the paper (figure 2(g)), but no charge transfer occurs in the open-circuit state. At this time, the potential difference between electrode 1 and electrode 2 reaches its maximum. The maximum positive voltage of the electrode can reach about +1500 V and the negative voltage about −1500 V. The simulation results are consistent with the experimental results. The potential difference between the two electrodes will gradually decrease with continuous rotation until the area of each electrode opposite the two friction media is equal (figure 2(h)) and the potential difference between the electrodes is minimum. At this time, the voltage potential difference between the two electrodes is close to 0. The constant displacement of the rotor will break the balance between the two electrodes at this moment, and the left electrode will start to display a negative voltage while the right electrode will start to display a positive voltage. Until the corresponding positions of electrode 1 and electrode 2 are exchanged, the potential difference between the two electrodes again reaches the maximum, but electrode 1 has a negative voltage at this time and electrode 2 a positive voltage. At this time, half of the voltage cycle is completed. With the rotation of the rotor, the potential difference between the two electrodes again decreases to 0 (figure 2(i)). Then the positive and negative voltages of the two electrodes are exchanged again until they return to their original positions (figure 2(g)). The whole process represents a complete voltage cycle.

### *2.3. Performance comparison of the TENG*

Based on the above theoretical analysis and finite element simulation results, we measured the current, voltage and charge transfer performance of soft-contact TENG devices, and compared the differences in performance between a direct-contact TENG and soft-contact TENG at different speeds.

The radius of the soft-contact TENG used in the experiment is 9 cm. The gap angle between electrodes is an important structural parameter that affects output performance. In our work, we found that a gap angle of 2°–10° can

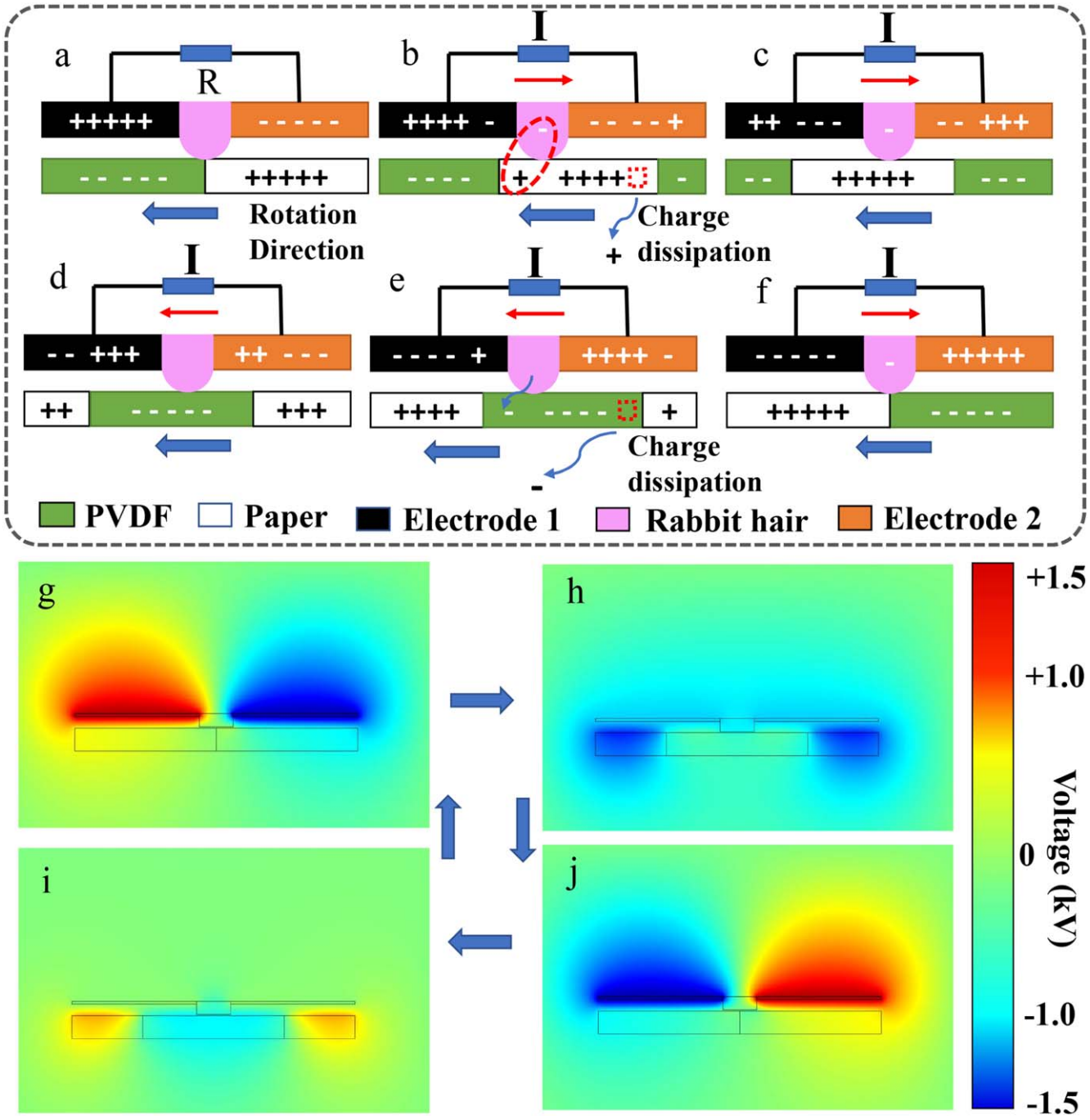


**Figure 2.** (a)–(f) Working mechanism of the soft-contact R-TENG. (g)–(j) Simulated potential distribution of two electrodes of the TENG under different working processes.

make the device output a higher voltage, so the gap angle of the device is set to 10°. [50] The TENG is driven by a programmable rotary motor to obtain an accurate speed. The short-circuit current ($I_{sc}$) of a high-performance soft-contact TENG has a steady AC signal at an amplitude of 12 $\mu$A. A partial magnified view is shown in figure 3(d). The signal characteristics of the sine wave sample are consistent with the previous theoretical analysis (figures 2(a)–(g)). The experimental voltage of the TENG is measured by the voltage divider method, and two resistors with resistance values of 100 M ($R_1$) and 100 G ($R_2$) are connected in series in the external circuit. The open-circuit voltage ($V_{oc}$) signal is shown in figure 3(b). The peak voltage of the AC signal can be seen to be as high as 1200 V. When compared with soft-contact and non-contact TENGs in other works (see figure S3), the output voltage of our TENG is much higher. This indicates that the performance of devices constructed with full-fiber structural materials can be improved [49, 51–53]. The experimental results are close to the previous simulation results (figures 2(g)–(j)). The amplification result for the open-circuit voltage is shown in figure 3(e). The waveform of the sine wave sample is similar to the short-circuit current.

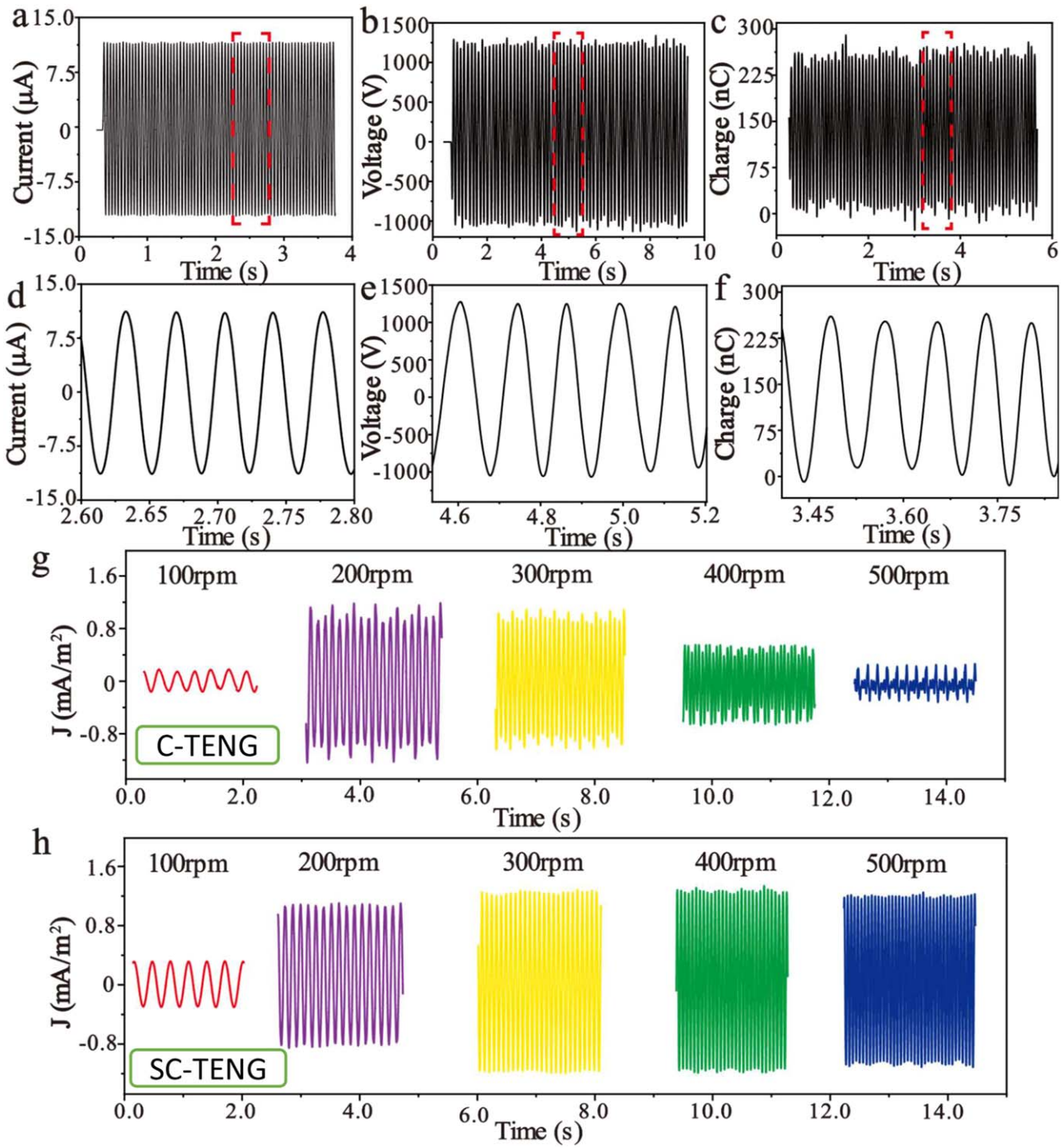


**Figure 3.** Performance comparison of a soft-contact R-TENG. (a), (d) Short-circuit current of the high-performance soft-contact TENG (a) and local enlarged drawing (d). (b), (e) Open circuit voltage of the high-performance soft-contact TENG (b) and local enlarged drawing (e). (c), (f) Transferred charge of the high-performance soft-contact TENG (c) and local enlarged drawing (f). (g) Current density of direct-contact TENG with different rotation speeds. (h) Current density of the high-performance soft-contact TENG with different rotation speeds.

The peak value of the transferred charge ($Q_{sc}$) is about 250 nC at the same rotational speed. An enlarged plot is shown in figure 3(f). All output signals are continuous, stable sinusoidal waveforms. This can be verified with the previous theoretical analysis.

These stable signals indicate that soft contact based on fiber materials can effectively guarantee sufficient friction, thus ensuring the excellent output performance of the TENG. On the other hand, the soft contact also avoids up and down vibration of the TENG rotor during rotation so it has good stability. The impact of such vibration will be more obvious in high-speed rotation. Compared with a direct-contact TENG, the soft-contact TENG has the advantages of long service life and stable output performance. Therefore, we

compared the changes in output performance of the two TENGs at different speeds. Figure 3(h) shows the output signal of a contact TENG with rotating speeds from 100 rpm to 500 rpm. As shown in the figure, when the speed is 100 rpm, the peak value and frequency of the output signal are very low. The output current reaches a maximum at 300 rpm, and then the speed does not increase the output but only the signal frequency. According to the formula for current definition (1)

$$i = \frac{dQ}{dt} \tag{1}$$

the current is inversely proportional to the length of the charge transfer period. The low speed means that it takes a long time for the two dielectrics of the rotor to exchange corresponding positions with the two electrodes of the stator, so the charge transfer cycle is long and the output is low. The higher the rotational speed, the shorter the charge transfer period. At high speeds, although the charge transfer cycle is shortened, the instability between the rotor and stator still causes a partial decrease in the amount of transferred charge. Therefore, even if the speed increases after 300 rpm, the output current will not increase. The amount of transferred charge corresponding to different rotation speeds of the soft-contact TENG (figure S2) clearly illustrates this problem.

The friction materials used for a direct-contact TENG are PVDF and paper, and the specific size parameters are consistent with those of the soft-contact TENG. The counterpart signals of a direct contacting TENG are shown in figure 3(g). Similar to the output signal of the soft-contact TENG, at 100 rpm the output signal is low and reaches a maximum at 300 rpm. However, further increase in the rotation speed will lead to a reduction in the signal of the direct-contact TENG, so that the output signal at 500 rpm is less than one-fifth of the maximum output value. This is due to the increased vibration and insufficient contact between the contact surfaces of the direct-contact TENG at high rotation speeds. On the one hand, the TENG's soft contact based on fiber materials can effectively guarantee a sufficiency of friction, thus ensuring an excellent output performance. On the other hand, the soft contact also avoids vibration of the R-TENG rotor during high-speed rotation to ensure its stability. We also conducted durability tests on the soft-contact TENG. The results are shown in figure S5, and after more than 100 000 cycles there was no significant change in TENG output, which could still exceed 10 $\mu$A. The TENG worked for 2 h a day and the output changes for 7 days were continuously measured. The results showed that after 7 days the output was still close to 10 $\mu$A. Despite a slight decrease in short-circuit current, the performance output overall remains relatively stable. Therefore, the device has good performance and long-term sustainability.

### *2.4. High-voltage output of the TENG*

The ternary dielectric triboelectric nanogenerator based on fiber structure, which has the advantage of high stability, shows excellent performance compared with previous reports [54–56]. TENGs have great potential as high-voltage power supplies based on high-voltage output. To broaden the range of applications of TENGs and change the characteristics of the AC output, appropriate circuit management needs to be used to modulate the output signal. The signal processed through a bridge rectifier, which is the most commonly used circuit for converting AC to DC, is shown in figure 4(a). It can be seen from the figure that the output signal only has a forward voltage with a peak value of about 1200 V. In addition, a voltage multiplication circuit containing diodes and capacitors was used, as shown in figure 4(b). The specific working principle and diagram of the management circuit are shown in the Supporting Information (figure S4). When the upper two terminals in the figure are output terminals, the output voltage will be twice the original TENG output voltage. Similarly, the tripled voltage will be output at the lower terminals. The double output signal processed by the circuit management system is shown in figure 4(c). It can be seen that the output peak value of the signal is about 2424 V after rectification and voltage doubling. An enlarged view of the peak voltage details is shown in figure S3. Similarly, figure 4(d) shows a test signal three times the original TENG voltage. In order to analyze the output stability, we calculated the crest factor under different conditions. The specific calculation process and results are shown in figure S7 and table S2. According to the results, the crest factor of the signal without any processing is 1.41, and the crest factor of the signal with a triple voltage multiplier circuit decreases to 1.31. The DC signal after voltage doubling rectification can continuously light up 2200 LED bulbs, as shown in figure S8 and supplementary video 3. There is no noticeable flickering of light or dark on the LED, indicating that the output of the soft-contact TENG after circuit management is already relatively close to a constant current. The continuous and stable high-voltage output shows that the TENG with circuit management is competent enough to be used as a high-voltage power supply.

To verify the high-voltage output characteristics of the device, we used it to conduct air breakdown with a breakdown device made of a glass tube and two tungsten metal needles and recorded the process with a high-speed camera. Figures 4(e)–(g) show the transient state before and after air breakdown. The air gap between the needle tips in the figure is about 1.5 mm. According to Paschen's law describing air breakdown voltage, a voltage of about 3440 V will cause tip discharge. Paschen's law is shown in formula (2)

$$V_b = \frac{Bpd}{\ln(Apd) - \ln\left(\ln\left(1 + \frac{1}{\gamma_{se}}\right)\right)} \tag{2}$$

where $d$ is the gap distance, $p$ is the operating pressure, $A$ and $B$ are constants determined by gas composition and $\gamma_{se}$ is the secondary electron emission coefficient (the parameters used in this equation are shown in table S1 in the Supporting Information). A magnified view of the moment when air breakdown occurs at the beginning is shown in figure 4(f); then a bright electric spark can be seen. The complete

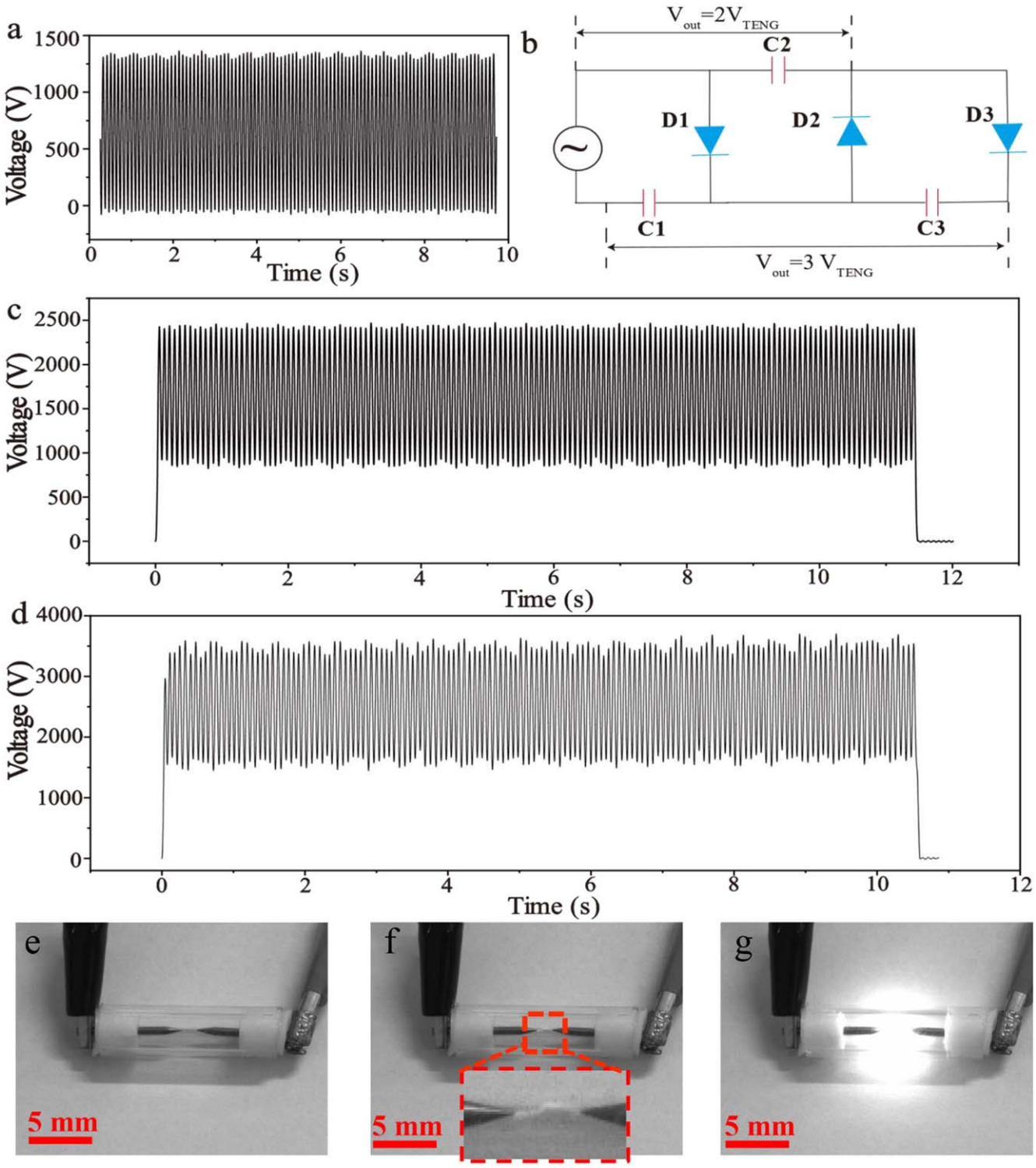


**Figure 4.** Output voltage improvement of the soft-contact R-TENG. (a) Electric circuit diagram of the voltage multiplier circuit for converting AC to DC with high voltage. (b) DC open-circuit voltage of the bridge rectifier. (c), (d) Output voltage with a voltage-doubler rectifier circuit (c) and a voltage-tripler rectifier circuit (d). (e), (f) Breakdown process caused by high voltage.

discharge process captured by the high-speed camera is shown in video 1 in the Supporting Information. The breakdown experiment proves that the output voltage of the TENG after circuit management can reach about 3440 V, which is consistent with the data measured in our experiment in figure 4(d).

### *2.5. Self-powered UV sterilization system*

Considering that many infectious diseases can easily spread in air, it is very important to develop an environmentally friendly method to kill bacteria. Ultraviolet sterilization has long been proven to be an efficient physical sterilization method. It mainly acts on the DNA or RNA of

microorganisms, destroying the genetic material structure and making it lose the function of reproduction and self-replication, thus achieving the aim of sterilization and disinfection. It has the advantages of simplicity, convenience, broad-spectrum efficiency, no secondary pollution, etc. An ultraviolet lamp made of a quartz glass tube is the most widely used and simple tool in daily ultraviolet sterilization. But starting the lamp requires high-voltage excitation, and the domestic electricity supply needs complex circuit conversion to drive it. Therefore, the portability of the lamp is greatly reduced and its use in outdoor or remote areas with an unreliable and inconvenient power supply is also limited. Due to the unique advantages of a TENG's high voltage and low current, the ultraviolet lamp directly driven by a TENG can be used for air sterilization. A demonstration of this application is illustrated in figure 5(a). The working principle of this self-powered ultraviolet sterilization system is shown in figure 5(b). The output of the TENG is driven by the energy management system shown in figure 4 to operate the quartz tube ultraviolet lamp. After the effects of both ultraviolet radiation and ozone, the bacterial content in the air will be reduced. To verify the universal bactericidal effect of the self-powered sterilization system, *Escherichia coli* was irradiated by the self-driving ultraviolet system within 0–40 min. The disinfection results are shown in figures 5(c) and (d). As shown, 793 colonies grew on the surface of the culture dish without irradiation after constant-temperature culturing for 24 h, and the number of colonies was reduced to less half after 20 min UV irradiation. After 40 min of treatment, there were very few viable bacteria left on the surface of the Petri dish, leaving only 69 colonies. The bactericidal rate reached 91.3%. Compared with the commonly used TENG-driven high-voltage breakdown sterilization method in existing reports, the use of TENG-driven ultraviolet tubes for disinfection makes the system more convenient [57]. The sterilization range is not limited to small-scale water sterilization and can be used for sterilization in households and other environments [58]. The statistical results for sterilization are shown in figure 5(g). The contrast of the ultraviolet lamp before and after lighting is shown in figures 5(f) and (g). More detailed video materials can be seen in the supplementary material video 2. It is worth noting that the main luminous spectral lines of the illuminated ultraviolet germicidal lamp are 254 nm and 185 nm. Ultraviolet light at 254 nm kills bacteria by irradiating their DNA, while 185 nm ultraviolet light can change $O_2$ in the air into $O_3$ (ozone). Ozone has a strong oxidation effect and can effectively kill bacteria. The dispersion of ozone can just make up for the shortcomings of ultraviolet light that only travels in a straight line and disinfects dead corners. Figure 5(h) shows that the ozone generated by the self-powered ultraviolet sterilization system will reach a concentration of 7 ppm when it works for about 10 min. It then reaches the required concentration for air disinfection. Therefore, under the dual action of ultraviolet and ozone, the sterilization system driven by a TENG can achieve a sterilization rate of 91.3% after 40 min of treatment. Compared with commonly used electric breakdown sterilization methods, ultraviolet sterilization is more convenient and has lower usage requirements.

## 3. Conclusions

In this paper we have developed a soft-contact fiber-structure TENG for driving Ar–Hg UV lamps with mobile disinfection and infectious disease control systems. Degradable and fiberous rabbit hair, paper and PVDF are used to build the friction medium of the soft-contact TENG to avoid insufficient friction states and to improve the output. Compared with a direct-contact TENG, the output performance of the soft-contact TENG at high speed (500 rpm) is improved by at least 350%, and the equipment operates stably. In addition, the abrasion of the dielectric surface is effectively reduced, and the service life of the TENG is greatly improved. Through the strategy of special circuit management, the TENG has achieved a 3440 V open-circuit voltage output. Finally, a TENG-driven ultraviolet sterilization system is used for indoor air environments to prevent bacterial propagation, which expands the application scope of TENG self-powered equipment in the prevention of infectious diseases.

## 4. Experimental section

### 4.1. Material

CNT solution (9–10 wt%), *N*,*N*-dimethylformamide (DMF) and acetone were purchased from Shanghai Aladdin Biochemical Technology Co., Ltd (Shanghai, China). PVDF was purchased from Shanghai Macklin Biochemical Co., Ltd (Shanghai, China). Paper, rabbit hair and acrylic were purchased from local stores.

### 4.2. Fabrication of the electrospinning PVDF film

One gram of PVDF was dispersed in 2 ml of acetone and 2 ml of DMF. The resultant solution was stirred for 8 h. With a voltage of 15 kV, PVDF fibers were spun on the acrylic substrate. The spinning environment temperature was 25 °C and the humidity 20%. The spraying speed was maintained at 1 ml $h^{-1}$ for 5 h. The distance between the acrylic base and the needle was 15 cm.

### 4.3. Fabrication of the CNTs electrodes

The diameter of the entire electrode was 180 mm. It comprises two parts: the inner electrode, defined as electrode 1, and the outer electrode, defined as electrode 2. The distance between the electrodes is 10°. First, the Kapton tape attached to the acrylic substrate was cut into the shape of electrode 1, electrode 2 and the gap using a laser cutter. The mask is the part remaining after removing the electrode shape. The radius of the innermost circle of the mask is 8 mm and that of the outermost circle 90 mm; the width of the arc part is 5 mm. Then the CNT solution was spin coated on the entire acrylic plate at 1000 rpm. The spin-coated electrode was kept in a 333 K oven for 2 h to cure. Finally, the mask was removed to leave the electrode part.

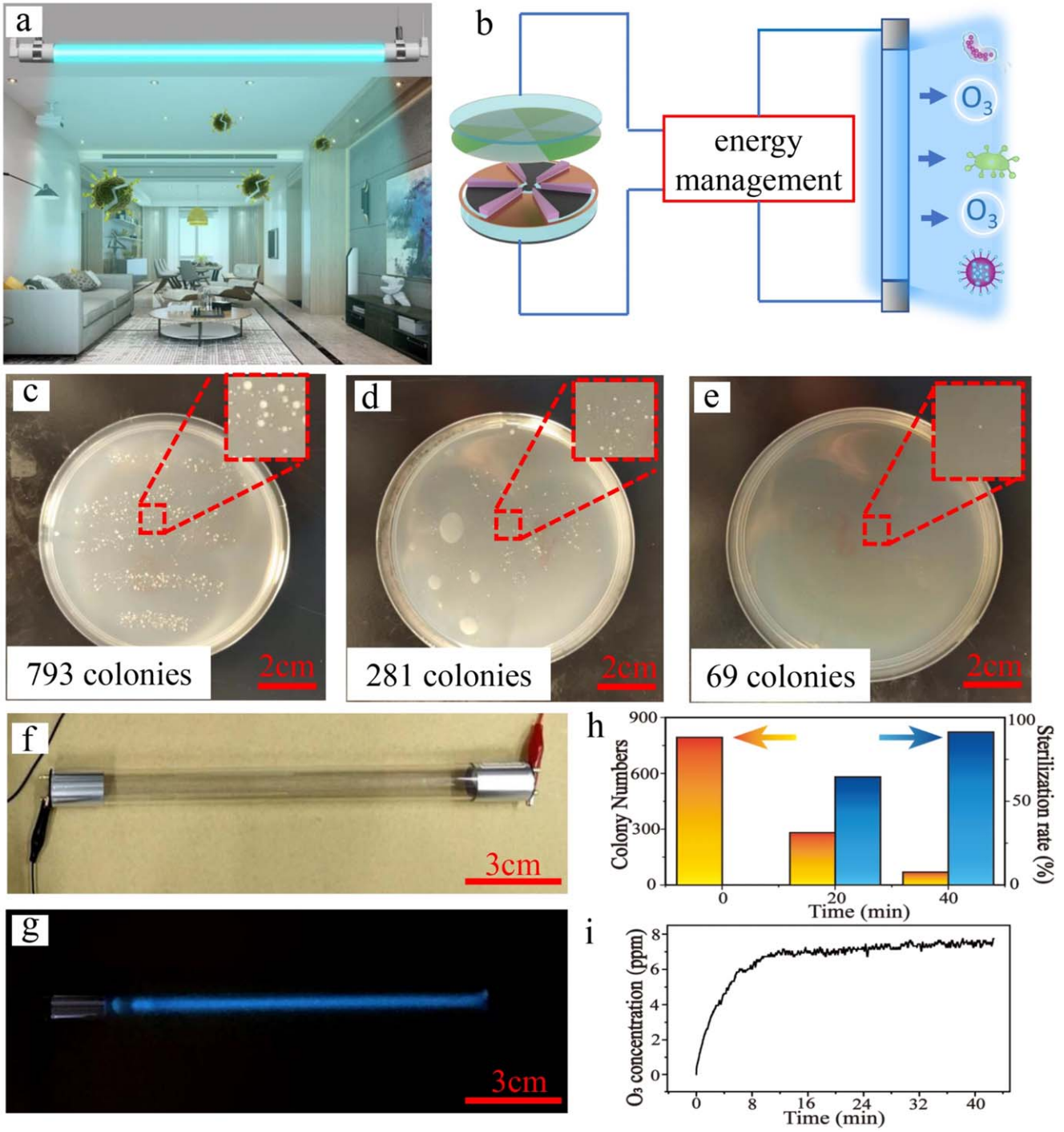


**Figure 5.** Self-powered UV sterilization system. (a) A proposed conceptual application of the TENG used for self-powered UV sterilization in an indoor environment. (b) Circuit schematic of disinfection with an Ar–Hg ultraviolet lamp driven by a TENG. (c)–(e) Photographs of *Escherichia coli* colonies under irradiation times of 0 min, 20 min and 40 min. The scale bar is 2 cm. (e), (f) Photograph of the Ar–Hg ultraviolet lamp that is directly powered by the TENG before and after luminescence, respectively. (g) Statistical results of sterilization. (h) The ozone concentration generated by the self-driven ultraviolet sterilization system.

### *4.4. Fabrication of the soft-contact R-TENG*

For the rotor part, the prepared PVDF spinning film was cut into six equal fan-shaped pieces using a laser cutter. The angle of every sector is 60°. Alternate sectors were removed, leaving three blank areas and three PVDF sectors arranged alternately. Then the paper was attached to the acrylic substrate in the blank area. For the stator part, the fan-shaped gaps between the electrodes were filled with rabbit hair.

### *4.5. Measurement*

The surface morphology of rabbit hair, paper, PVDF spinning film and CNTs was characterized by scanning electron

microscopy (SEM; Carl Zeiss AG Gemini300). An electrometer (Keithley 6514) was used to test the load voltage by the series resistance divider method. The current was measured using a low-noise current preamplifier (Stanford Research System, model SR570). A motor (PERFECT, 5RK120RGU-CF) was used to drive the rotor of the high-performance TENG. The ozone concentration was measured with an ozone ($O_3$) transmitter (Shandong RENZHICEKONG Co., Ltd).

## Acknowledgments

The research is supported by the Fundamental Research Funds for the Natural Science Foundation of Shandong Province, China (no. ZR2021QE043), National Natural Science Foundation of China (no. 52101390), Central Universities, China (no. 202112011), Joint Funds of National Natural Science Foundation of China (no. U2106216), Open Project of Key Lab of Special Functional Materials of Ministry of Education, Henan University (KFKT-2022–11).

## Data availability statement

All data that support the findings of this study are included within the article (and any supplementary files).

## Author contributions

Jianwei He: data curation, formal analysis, investigation, validation, writing—original draft. Xuhua Guo: data curation, formal analysis, investigation, validation, writing—original draft. Caofeng Pan, Gang Cheng, Mingli Zheng and Yunlong Zi: resources, supervision. Hongzhi Cui: resources, funding acquisition, supervision. Xiaoyi Li: conceptualization, resources, funding acquisition, supervision, writing—review and editing.

## Conflicts of interest

There are no conflicts to declare.

## ORCID iDs

Caofeng Pan https://orcid.org/0000-0001-6327-9692
Gang Cheng https://orcid.org/0000-0002-1242-8739
Xiaoyi Li https://orcid.org/0000-0001-5082-6757

## References

[1] Cohn S K Jr and Weaver L T 2006 The black death and AIDS: CCR5-DELTA32 in genetics and history *QJM: Mon. J. Assoc. Physicians* **99** 497–503
[2] Wear A and Hays J N 2000 The burdens of disease: epidemics and human response in western history *Am. Hist. Rev.* **105** 580–1
[3] Sena G R *et al* 2021 Clinical characteristics and mortality profile of COVID-19 patients aged less than 20 years old in Pernambuco - Brazil *Am. J. Trop. Med. Hyg.* **104** 1507–12
[4] Cervia C *et al* 2021 Systemic and mucosal antibody responses specific to SARS-CoV-2 during mild versus severe COVID-19 *J. Allergy Clin. Immunol.* **147** 545–57
[5] Bloom D E and Cadarette D 2019 Infectious disease threats in the twenty-first century: strengthening the global response *Front. Immunol.* **10** 549
[6] Smith K F, Goldberg M, Rosenthal S, Carlson L, Chen J, Chen C and Ramachandran S 2014 Global rise in human infectious disease outbreaks *J. R. Soc. Interface* **11** 20140950
[7] Morens D M and Fauci A S 2013 Emerging infectious diseases: threats to human health and global stability *PLoS Pathog.* **9** e1003467
[8] Ong S W X *et al* 2022 Transmission modes of severe acute respiratory syndrome coronavirus 2 and implications for infection control: a review *Singapore Med. J.* **63** 61–7
[9] Ng O W, Chia A, Tan A T, Jadi R S, Leong H N, Bertoletti A and Tan Y J 2016 Memory T cell responses targeting the SARS coronavirus persist up to 11 years post-infection *Vaccine* **34** 2008–14
[10] Donnelly C A *et al* 2003 Epidemiological determinants of spread of causal agent of severe acute respiratory syndrome in Hong Kong *Lancet* **361** 1761–6
[11] Lee D-H, Torchetti M K, Winker K, Ip H S, Song C-S and Swayne D E 2015 Intercontinental spread of Asian-origin H5N8 to North America through Beringia by migratory birds *J. Virol.* **89** 6521–4
[12] Garske T, Legrand J, Donnelly C A, Ward H, Cauchemez S, Fraser C, Ferguson N M and Ghani A C 2009 Assessing the severity of the novel influenza A/H1N1 pandemic *BMJ* **339** b2840
[13] Remington P L, Hall W N, Davis I H, Herald A and Gunn R A 1985 Airborne transmission of measles in a physician's office *JAMA* **253** 1574–7
[14] Stephens D S, Greenwood B and Brandtzaeg P 2007 Epidemic meningitis, meningococcaemia, and *Neisseria meningitidis* *Lancet.* **369** 2196–210
[15] Turner R D and Bothamley G H 2015 Cough and the transmission of tuberculosis *J. Infect. Dis.* **211** 1367–72
[16] Chitnis A S, Davis J L, Schecter G F, Barry P M and Flood J M 2015 Review of nucleic acid amplification tests and clinical prediction rules for diagnosis of tuberculosis in acute care facilities *Infect. Control Hospital Epidemiol.* **36** 1215–25
[17] Peng Z *et al* 2022 Correction to practical indicators for risk of airborne transmission in shared indoor environments and their application to COVID-19 outbreaks *Environ. Sci. Technol.* **56** 3302–3
[18] Hora P I, Pati S G, McNamara P J and Arnold W A 2020 Increased use of quaternary ammonium compounds during the SARS-CoV-2 pandemic and beyond: consideration of environmental implications *Environ. Sci. Technol. Lett.* **7** 622–31
[19] Yang M and Zhang X 2013 Comparative developmental toxicity of new aromatic halogenated DBPs in a chlorinated saline sewage effluent to the marine polychaete *Platynereis dumerilii Environ. Sci. Technol.* **47** 10868–76
[20] Wang Z 2020 On the first principle theory of nanogenerators from Maxwell's equations *Nano Energy* **68** 104272
[21] Li X, Lau T H, Guan D and Zi Y 2019 A universal method for quantitative analysis of triboelectric nanogenerators *J. Mater. Chem.* A **7** 19485–94
[22] Fan F, Tian Z and Wang Z 2012 Flexible triboelectric generator *Nano Energy* **1** 328–34

[23] Yang Z, Liu T, Wu J, Xu T, Wang X, Han X, Cui H, Xu X, Pan C and Li X 2022 Energy conversion analysis of multilayered triboelectric nanogenerators for synergistic rain and solar energy harvesting *Adv. Mater.* **34** 2202238

[24] He T, Wang H, Wang J, Tian X, Wen F, Shi Q, Ho J S and Lee C 2019 Self-sustainable wearable textile nano-energy nano-system (NENS) for next-generation healthcare applications *Adv. Sci.* **6** 1901437

[25] Fan F R, Tang W and Wang Z L 2016 Flexible nanogenerators for energy harvesting and self-powered electronics *Adv. Mater.* **28** 4283–305

[26] Zhang X, Han M, Wang R, Zhu F, Li Z, Wang W and Zhang H 2013 Frequency-multiplication high-output triboelectric nanogenerator for sustainably powering biomedical microsystems *Nano Lett.* **13** 1168–72

[27] Xu L, Jiang T, Lin P, Shao J J, He C, Zhong W, Chen X Y and Wang Z L 2018 Coupled triboelectric nanogenerator networks for efficient water wave energy harvesting *ACS Nano* **12** 1849–58

[28] Li X, Tao J, Wang X, Zhu J, Pan C and Wang Z L 2018 Networks of high performance triboelectric nanogenerators based on liquid–solid interface contact electrification for harvesting low-frequency blue energy *Adv. Energy Mater.* **8** 1800705

[29] Wang Z L, Jiang T and Xu L 2017 Toward the blue energy dream by triboelectric nanogenerator networks *Nano Energy* **39** 9–23

[30] Li X, Tao J, Zhu J and Pan C 2017 A nanowire based triboelectric nanogenerator for harvesting water wave energy and its applications *APL Mater.* **5** 074104

[31] Lin Z, Cheng G, Lin L, Lee S and Wang Z L 2013 Water–solid surface contact electrification and its use for harvesting liquid-wave energy *Angew. Chem. Int. Ed.* **52** 12545–9

[32] Zhou Z, Peng W, Jiawei L, Congyu W, Junhuan C, Liyang Z, Haitao Z and Dun Z 2022 A self-powered microbiosensor system for specific bacteria detection based on triboelectric nanogenerator *Nano Energy* **98** 107317

[33] Wang C, Wang P, Chen J, Zhu L, Zhang D, Wan Y and Ai S 2022 Self-powered biosensing system driven by triboelectric nanogenerator for specific detection of Gram-positive bacteria *Nano Energy* **93** 106828

[34] Zhang D, Wang D, Xu Z, Zhang X, Yang Y, Guo J, Zhang B and Zhao W 2021 Diversiform sensors and sensing systems driven by triboelectric and piezoelectric nanogenerators *Coord. Chem. Rev.* **427** 213597

[35] Wu J, Zheng Y and Li X 2021 Recent progress in self-powered sensors based on triboelectric nanogenerators *Sensors* **21** 7129

[36] Zhao G, Zhang Y, Shi N, Liu Z, Zhang X, Wu M, Pan C, Liu H, Li L and Wang Z 2019 Transparent and stretchable triboelectric nanogenerator for self-powered tactile sensing *Nano Energy* **59** 302–10

[37] Chen J, Wang P, Li J, Wang C, Wang J, Zhang D, Peng Y, Wang B and Wu Z 2022 Self-powered antifouling UVC pipeline sterilizer driven by the discharge stimuli based on the modified freestanding rotary triboelectric nanogenerator *Nano Energy* **95** 106969

[38] Li Q, Liu W, Yang H, He W, Long L, Wu M, Zhang X, Xi Y, Hu C and Wang Z L 2021 Ultra-stability high-voltage triboelectric nanogenerator designed by ternary dielectric triboelectrification with partial soft-contact and non-contact mode *Nano Energy* **90** 106585

[39] Lei R, Shi Y, Ding Y, Nie J, Li S, Wang F, Zhai H, Chen X and Wang Z 2020 Sustainable high-voltage source based on triboelectric nanogenerator with a charge accumulation strategy *Energy Environ. Sci.* **13** 2178–90

[40] Tian J *et al* 2017 A self-powered sterilization system with both instant and sustainable anti-bacterial ability *Nano Energy* **36** 241–9

[41] Zhang X, Huang H, Zhang W, Hu Z, Li X, Liu J, Xu G and Yang C 2022 Self-powered triboelectric nanogenerator driven nanowires electrode array system for the urine sterilization *Nano Energy* **96** 107111

[42] Chen J, Li J, Wang P, Peng Y, Wang C, Wang J and Zhang D 2023 Utilizing breakdown discharge of self-powered triboelectric nanogenerator to realize multimodal sterilization *Adv. Sustain. Syst.* **7** 2200383

[43] Chen J, Wei X, Wang B, Li R, Sun Y, Peng Y, Wu Z, Wang P and Wang Z L 2021 Design optimization of soft-contact freestanding rotary triboelectric nanogenerator for high-output performance *Adv. Energy Mater.* **11** 2102106

[44] Li X, Tao J, Zhu J and Pan C 2017 A nanowire based triboelectric nanogenerator for harvesting water wave energy and its applications *APL Mater.* **5** 074104

[45] Luo J, Han K, Wu X, Cai H, Jiang T, Zhou H and Wang Z L 2021 Self-powered mobile sterilization and infection control system *Nano Energy* **88** 106313

[46] Chen P F, An J, Shu S, Cheng R W, Nie J H, Jiang T and Wang Z L 2021 Super-durable, low-wear, and high-performance fur-brush triboelectric nanogenerator for wind and water energy harvesting for smart agriculture *Adv. Energy Mater.* **11** 2003066

[47] Wu Z, Cheng T and Wang Z L 2020 Self-powered sensors and systems based on nanogenerators *Sensors* **20** 2925

[48] Lin Z, Zhang B, Zou H, Wu Z, Guo H, Zhang Y, Yang J and Wang Z 2020 Rationally designed rotation triboelectric nanogenerators with much extended lifetime and durability *Nano Energy* **68** 104378

[49] Chen J, Guo H, Hu C and Wang Z 2020 Robust triboelectric nanogenerator achieved by centrifugal force induced automatic working mode transition *Adv. Energy Mater.* **10** 2000886

[50] Guo X, He J, Zheng Y, Wu J, Pan C, Zi Y, Cui H and Li X 2023 High-performance triboelectric nanogenerator based on theoretical analysis and ferroelectric nanocomposites and its high-voltage applications *Nano Res. Energy* **2** 9120074

[51] Lin Z, Zhang B, Zou H, Wu Z, Guo H, Zhang Y, Yang J and Wang Z L 2020 Rationally designed rotation triboelectric nanogenerators with much extended lifetime and durability *Nano Energy* **68** 104378

[52] Long L, Liu W, Wang Z, He W, Li G, Tang Q, Guo H, Pu X, Liu Y and Hu C 2021 High performance floating self-excited sliding triboelectric nanogenerator for micro mechanical energy harvesting *Nat. Commun.* **12** 4689

[53] Huo Z Y, Lee D M, Jeong J M, Kim Y J, Kim J, Suh I Y, Xiong P and Kim S W 2022 Microbial disinfection with supercoiling capacitive triboelectric nanogenerator *Adv. Energy Mater.* **12** 2103680

[54] Han J, Feng Y, Chen P, Liang X, Pang H, Jiang T and Wang Z L 2021 Wind-driven soft-contact rotary triboelectric nanogenerator based on rabbit fur with high performance and durability for smart farming *Adv. Funct. Mater.* **32** 2108580

[55] Feng H *et al* 2021 An ultra-simple charge supplementary strategy for high performance rotary triboelectric nanogenerators *Small* **17** 2101430

[56] Chen P, An J, Cheng R, Shu S, Berbille A, Jiang T and Wang Z L 2021 Rationally segmented triboelectric nanogenerator with a constant direct-current output and low crest factor *Energy Environ. Sci.* **14** 4523–32

[57] Cai C, Luo B, Liu T, Gao C, Zhang W, Chi M, Meng X and Nie S 2022 Triboelectric pulsed direct current for self-powered sterilization of cellulose fiber *Cellulose* **29** 7139–49

[58] Ding W, Zhou J, Cheng J, Wang Z, Guo H, Wu C, Xu S, Wu Z, Xie X and Wang Z L 2019 Tribopump: a low-cost, hand-powered water disinfection system *Adv. Energy Mater.* **9** 1901320